Anisotropic linear and nonlinear excitonic optical properties of buckled monolayer semiconductors

M. F. C. Martins Quintela [1,2,3,*] and T. Garm Pedersen [3]

[1] *Department of Physics, Physics Center of Minho, Porto Universities (CF–UM–UP), Campus of Gualtar, 4710-057 Braga, Portugal*

[2] *International Iberian Nanotechnology Laboratory (INL), Avenida Mestre José Veiga, 4715-330 Braga, Portugal*

[3] *Department of Materials and Production, Aalborg University, 9220 Aalborg Øst, Denmark*

(Received 19 April 2023; accepted 8 June 2023; published 20 June 2023)

The optical properties of two-dimensional materials are exceptional in several respects. They are highly anisotropic and frequently dominated by excitonic effects. Dipole-allowed second-order nonlinear optical properties require broken inversion symmetry. Hence, several two-dimensional materials show strong in-plane (IP) nonlinearity but negligible out-of-plane (OOP) response due to vertical symmetry. By considering buckled hexagonal monolayers, we analyze the critical role of broken vertical symmetry on their excitonic optical response. Both linear as well as second-order shift current and second-harmonic response are studied. We demonstrate that substantial OOP nonlinear response can be obtained, in particular, through off-diagonal tensor elements coupling IP excitation to OOP response. Our findings are explained by excitonic selection rules for OOP response and the impact of dielectric screening on excitons is elucidated.

DOI: 10.1103/PhysRevB.107.235416

I. INTRODUCTION

The recent interest in layered materials with broken vertical symmetry, such as Janus materials [1–3], buckled monolayers [4–7], as well as heterobilayers and biased homobilayers [8–11] makes the discussion on the effects of broken vertical symmetry on the optical response especially relevant [12–18]. The amplitude of both linear and nonlinear out-of-plane (OOP) conductivities is expected to be greatly dependent on the asymmetry of the layer with the even-order nonlinear OOP response being identically zero (within the dipole approximation) when the OOP symmetry is not broken. Hence, the broken OOP symmetry is crucial when one wishes to consider potential applications beyond those allowed by symmetric structures. The OOP nonlinear response in Janus monolayers has also been experimentally studied [19,20], namely, for both second–and third harmonics. This study was performed via polarization-resolved spectroscopy with the aim of mapping the full second-order susceptibility tensor [21–23] of MoSSe. These OOP nonlinearities then lead to additional degrees of freedom in vertical photonics structures [24,25], allowing for novel approaches in the design of ultrafast optical devices [26], such as miniaturized logic gates [27,28], nonlinear holograms [29], broadband ultrafast frequency converters [30,31], among others.

The simplest family of materials with broken OOP symmetry is that of buckled monolayer structures with theoretical predictions of both monoelemental and binary graphenelike materials [4,6,7], and several buckled hexagonal sheets (see Fig. 1) have already been fabricated. Among these materials, we mention specifically the monoelemental silicene [4,32], blue phosphorene [33], arsenene [34,35], antimonene [34,36], and bismuthene [37], as well as the binary CS, SiO, GeSe, SnTe, InSb, and GaAs [4,38]. The monoelemental structures preserve inversion symmetry even in the presence of buckling and, hence, possess negligible second-order nonlinearities. The band gaps of these materials can be both mechanically [39,40] or electrically [40,41] tuned, and they allow for potential applications is various fields, such as optoelectronics, spin electronics, sensors, and thermoelectrics [42–45].

The aim of the present paper is to understand the effects of both in-plane (IP) and OOP asymmetry on the excitonic optical response of honeycomb lattice structures. To this end, we consider a simple two-band model of gapped graphene near the so-called Dirac valleys [46–48] and then apply a small buckling to break OOP symmetry. To study IP even–order nonlinear optical properties [49–52], such as second-harmonic generation (SHG) [51,53] or shift–current (SC) [54–57], we include a quadratic (in k) contribution to the nearest-neighbor hopping function [58], namely, trigonal warping [59], plus distinct on-site potentials for the two sublattices. Including trigonal warping allows us to compute the IP even-order response, which then serves as a comparison against the OOP response.

This paper is organized as follows. In Sec. II, we will consider the single-particle Hamiltonian for gapped graphene whereas introducing trigonal warping before computing explicit matrix elements of the momentum and Berry connection. In Sec. III, we discuss the Bethe-Salpeter equation for the computation of the excitonic states. We also outline some of the approximations necessary for an efficient numerical solution of this equation. In Sec. IV, we briefly outline the general form of both the excitonic linear and the nonlinear optical response to linearly polarized light, discussing the momentum matrix elements between excitonic states. Finally, in Sec. V, we analyze the IP and OOP optical selection rules of a buckled graphene lattice structure (Fig. 1) which, in turn,

*mfcmquintela@gmail.com

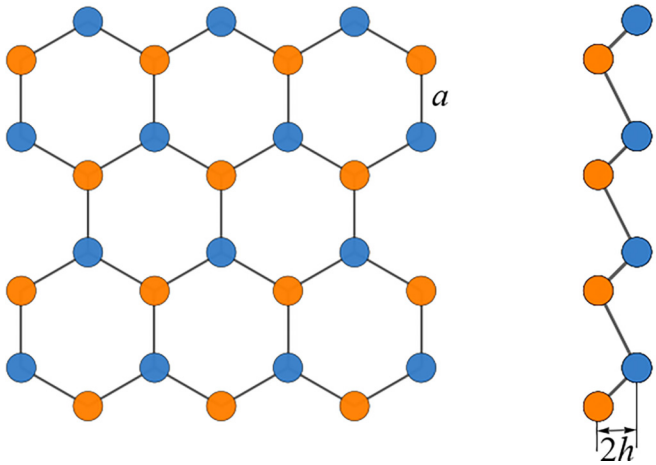

FIG. 1. Schematic of a buckled honeycomb lattice, highlighting the lattice constant a and the buckling h.

leads to a non–zero OOP excitonic response in the monolayer. The nonlinear response will be very sensitive to the scale of this buckling, quickly vanishing as the buckling decreases. We also compare both diagonal (σ_{zzz}) and nondiagonal ($\sigma_{zxx/xzx}$) components of the second-order excitonic conductivity tensor against their IP counterparts, discussing both their relative magnitudes and the location of the excitonic resonances.

II. SINGLE-PARTICLE GAPPED GRAPHENE HAMILTONIAN

Throughout this paper, we will work with a two-band model of gapped graphene near the Dirac points K/K' with the x axis aligned with the unit cell of the honeycomb lattice and the z axis perpendicular to the monolayer plane. The basis states are p_z orbitals on the two sublattices, and the model Hamiltonian before Dirac point expansion then reads

$$\mathcal{H}(\mathbf{k}) = \begin{bmatrix} \Delta & -\gamma f^*(\mathbf{k}) \\ -\gamma f(\mathbf{k}) & -\Delta \end{bmatrix}, \tag{1}$$

where $\pm\Delta$ is the staggered on-site energy, and γ the effective hopping. In this paper, we ignore spin effects and, as such, all spectra will be multiplied by spin and valley degeneracies. If spin-orbit interaction is considered, gap Δ becomes spin and valley dependent, meaning that the resulting spectra will have A and B components split by spin–orbit coupling [60]. Although for planar gapped graphene, the π and σ orbitals are decoupled, the vertical shift of the two sublattices in a buckled system means that the p_z orbitals are no longer on the same plane. Hence, the effective hopping will change as [61,62]

$$-\gamma = V_{pp\pi} + \frac{1}{1+\frac{a^2}{12h^2}}(V_{pp\sigma} - V_{pp\pi}), \tag{2}$$

where a is the lattice parameter, h is the buckling parameter, and $V_{pp\pi}$ and $V_{pp\sigma}$ are the hopping integrals for π and σ orbitals, respectively. As we are interested in a general model for small h/a, we will ignore $\pi-\sigma$ hybridization when computing the OOP response as we consider the OOP buckling to be much smaller than the lattice constant, taking the approximation $-\gamma \approx V_{pp\pi}$. The wave-vector-dependent function f is obtained from the honeycomb lattice geometry as

$$f(\mathbf{k}) = e^{ik_x a/\sqrt{3}} + 2e^{-ik_x a/(2\sqrt{3})}\cos\left(\frac{k_y a}{2}\right).$$

Expanding $f(\mathbf{k})$ near the Dirac points K/K' up to linear order, we obtain the massive Dirac Hamiltonian that is usually employed to study gapped graphene and hexagonal boron nitride (hBN) systems. Considering now an expansion up to quadratic order in k, we obtain [59]

$$f(\mathbf{k}) \approx \frac{\sqrt{3}a}{2}[(k_x + i\tau k_y) + i\zeta_{\mathrm{TW}} a(k_x - i\tau k_y)^2], \tag{3}$$

where $\tau = \pm 1$ is the valley index and $\zeta_{\mathrm{TW}} = \frac{\sqrt{3}}{12}$ is the trigonal warping strength. Although this trigonal warping strength is a fixed numerical factor, it is useful to keep it as a variable to enable systematic expansions in orders of ζ_{TW}.

A. Diagonalization

Diagonalizing Hamiltonian Eq. (1), we obtain the band structure as $\pm E$ with

$$E = \sqrt{\Delta^2 + \gamma^2 |f(\mathbf{k})|^2}. \tag{4}$$

As we are interested in linear contributions from trigonal warping, we approximate E up to first order in ζ_{TW} as

$$E \approx \varepsilon + \tau\frac{\xi}{\varepsilon}\zeta_{\mathrm{TW}}, \tag{5}$$

where

$$\varepsilon = \sqrt{\Delta^2 + \hbar^2 v_F^2 k^2},$$
$$\xi = a\hbar^2 v_F^2 k^3 \sin(3\theta), \tag{6}$$

with θ as the polar angle of the $\mathbf{k}$ vector and the Fermi velocity is defined as $v_F = \frac{1}{\hbar}\frac{\sqrt{3}a\gamma}{2}$. We then write the normalized eigenvectors as

$$|v_{\mathbf{k}}\rangle = \sqrt{\frac{E+\Delta}{2E}}\begin{bmatrix} \frac{e^{-i\tau\theta}(E-\Delta)}{\hbar v_F k(1+iak\zeta_{\mathrm{TW}}e^{-3i\theta\tau})} \\ 1 \end{bmatrix}, \tag{7}$$

$$|c_{\mathbf{k}}\rangle = \sqrt{\frac{E-\Delta}{2E}}\begin{bmatrix} \frac{-E-\Delta}{\hbar v_F k(1+iak\zeta_{\mathrm{TW}}e^{-3i\theta\tau})} \\ e^{i\tau\theta} \end{bmatrix}, \tag{8}$$

where v/c corresponds to the valence and conduction bands, respectively. From Eqs. (7) and (8), it is clear which components go to zero as $k \to 0$ as $E \approx \Delta + O(k^2)$ for small k, whereas, the denominators of the fraction in square brackets are $O(k)$.

The presence of the phase terms in spinor components that go to zero as $k \to 0$ in $|v_{\mathbf{k}}\rangle$ and $|c_{\mathbf{k}}\rangle$ will lead to a pseudospin angular quantum number $m_s = 0$ [8,63–67]. This pseudospin angular quantum number is governed by the phase choice and allows a direct association with the usual hydrogenlike states.

B. Momentum matrix element and Berry connection

The IP interband momentum matrix element in the i direction is defined as

$$p^i_{vc\mathbf{k}} = \langle v_\mathbf{k}| \frac{m}{\hbar}\frac{\partial \mathcal{H}(\mathbf{k})}{\partial k_i}|c_\mathbf{k}\rangle, \tag{9}$$

with m as the bare electron mass. When considering IP properties, we will focus our attention solely on the x direction as the inversion symmetry of the lattice along the y direction means that the yyy component of the nonlinear conductivity tensor will be trivially zero after summing over valley index. Alongside with the momentum matrix elements, we will also require Berry connections, defined as

$$\Omega^\alpha_{nm\mathbf{k}} = i\langle n_\mathbf{k}|\frac{\partial}{\partial k_\alpha}|m_\mathbf{k}\rangle, \tag{10}$$

as their explicit expression will play an important part in computing generalized derivatives [68].

To obtain the nonlinear conductivity tensor, we will consider incident fields with frequencys ω_p and ω_q. The indices for the current vector $\mathbf{J}^{(2)}(\omega_{pq})$ will contract as [51]

$$J^{(2)}_i(\omega_{pq}) = \sum_{j,k}\sigma^{(2)}_{ijk}(\omega_{pq};\omega_p,\omega_q)E_j(\omega_p)E_k(\omega_q), \tag{11}$$

where exchanging p and q implies an exchange of j and k indices. In contracted matrix notation [19] and with this in mind, we write

$$\begin{bmatrix} J^{(2)}_x(\omega_{pq}) \\ J^{(2)}_y(\omega_{pq}) \\ J^{(2)}_z(\omega_{pq}) \end{bmatrix} = \sigma^{(2)} \begin{bmatrix} E_x(\omega_p)E_x(\omega_q) \\ E_y(\omega_p)E_y(\omega_q) \\ E_z(\omega_p)E_z(\omega_q) \\ E_y(\omega_p)E_z(\omega_q) + (p \leftrightarrow q) \\ E_x(\omega_p)E_z(\omega_q) + (p \leftrightarrow q) \\ E_x(\omega_p)E_y(\omega_q) + (p \leftrightarrow q) \end{bmatrix}, \tag{12}$$

with $\mathbf{E}(\omega)$ as the external optical field, $\sigma^{(2)}$ the nonlinear conductivity matrix with matrix elements $\sigma^{(2)}_{ijk}(\omega_{pq};\omega_p,\omega_q)$, and the frequency $\omega_{pq} = \omega_p + \omega_q$. A simple symmetry analysis [19] tells us that the relevant components of the nonlinear conductivity tensor will be

$$\sigma^{(2)} = \begin{bmatrix} \sigma^{(2)}_{xxx} & -\sigma^{(2)}_{xxx} & 0 & 0 & \sigma^{(2)}_{xxz} & 0 \\ 0 & 0 & 0 & \sigma^{(2)}_{xxz} & 0 & -\sigma^{(2)}_{xxx} \\ \sigma^{(2)}_{zxx} & \sigma^{(2)}_{zxx} & \sigma^{(2)}_{zzz} & 0 & 0 & 0 \end{bmatrix}.$$

Compared to Ref. [59], we apply a simple relabeling of the two valleys ($\tau \to -\tau$) and the gauge change $|c_\mathbf{k}\rangle \to e^{i\tau\theta}|c_\mathbf{k}\rangle$. Although this gauge change leads to a global phase in the momentum matrix elements, it is important to note that the k_x derivative in the definition of the Berry connection will lead to a more complex transformation. Nonetheless, this is just a gauge choice and, therefore, both the free-carrier and the excitonic conductivities will be independent of this choice.

C. Free-carrier conductivity

When discussing both linear and nonlinear excitonic conductivities, we will include results for very large dielectric constants. In this limit, the excitonic response agrees with the free-carrier expression, obtained by computing the electronic conductivity in the free-carrier (single-particle) regime.

The generic expression for the free-carrier linear electronic conductivity in a clean two-band semiconductor at $T = 0$ is given by [68–72]

$$\sigma_{\alpha\beta}(\omega) = \frac{e^2\hbar}{i\pi^2 m^2}\left[\int \frac{p^\alpha_{vc\mathbf{k}}p^\beta_{cv\mathbf{k}}}{E_{cv\mathbf{k}}(E_{cv\mathbf{k}} - \hbar\omega)}d^2\mathbf{k} - (\omega \to -\omega)^*\right], \tag{13}$$

where $E_{cv\mathbf{k}} = 2E$ and the integration runs over the Brillouin zone. Analogously, the generic intraband nonlinear electronic conductivity in a clean two-band semiconductor can be written as [68–72]

$$\sigma^{(\text{intra})}_{\alpha\beta\lambda}(\omega_p,\omega_q) = \frac{e^3\hbar^2(\omega_p+\omega_{pq})}{2\pi^2 m^2} \times \int \frac{p^\alpha_{vc\mathbf{k}}\left[p^\beta_{cv\mathbf{k}}\right]_{;k_\lambda}}{\left(E^2_{cv\mathbf{k}} - \hbar^2\omega_p^2\right)\left(E^2_{cv\mathbf{k}} - \hbar^2\omega^2_{pq}\right)}d^2\mathbf{k} + \begin{pmatrix} p \leftrightarrow q \\ \beta \leftrightarrow \lambda \end{pmatrix}, \tag{14}$$

where $[p^\beta_{cv\mathbf{k}}]_{;k_\lambda}$ is the generalized derivative [68] in the λ irection of the momentum matrix element for the β direction, defined as

$$\left[p^\beta_{cv\mathbf{k}}\right]_{;k_\lambda} = \frac{\partial p^\beta_{cv\mathbf{k}}}{\partial k_\lambda} - i\left(\Omega^\lambda_{cc\mathbf{k}} - \Omega^\lambda_{vv\mathbf{k}}\right)p^\beta_{cv\mathbf{k}}. \tag{15}$$

When considering $\lambda = z$, the k_z derivative term in Eq. (15) is discarded as there is no dependence on k_z in the momentum matrix elements. The specific details for the calculation of both $p^z_{vc\mathbf{k}}$ and $\Omega^z_{nm\mathbf{k}}$ will be discussed in Sec. V.

Although the integrals of Eqs. (13) and (14) are over the entire Brillouin zone, performing the expansion around the Dirac points means that the integration is now over the infinite Dirac cone and that a sum over valleys must be made. Due to the smallness of ζ_{TW}, we are interested contributions up to $O(\zeta_{\text{TW}})$. The ζ_{TW} factor must come from either $E_{cv\mathbf{k}}$ or $p^\alpha_{vc\mathbf{k}}[p^\beta_{cv\mathbf{k}}]_{;k_\lambda}$. Time-reversal symmetry means that $E_{cv\mathbf{k}} = E_{cv-\mathbf{k}}$. Any term containing $p^\alpha_{vc\mathbf{k}}[p^\beta_{cv\mathbf{k}}]_{;k_\lambda}$ to zeroth order in ζ_{TW} will vanish upon integration and summation over the valley. This allows us to set $E_{cv\mathbf{k}} = 2\varepsilon$ whereaas retaining $O(\zeta_{\text{TW}})$ contribution to $p^\alpha_{vc\mathbf{k}}[p^\beta_{cv\mathbf{k}}]_{;k_\lambda}$ throughout this paper when computing the various transition amplitudes. These integrals can be computed analytically in our first-order approximation in ζ_{TW} with the exact expressions present in Appendix B for the various processes considered.

III. BETHE-SALPETER EQUATION

Before discussing the excitonic conductivity, we must first compute the excitonic states for each τ valley. To compute the excitonic wave functions and their binding energies, we will solve the Bethe-Salpeter equation [59,66,72,73], given in

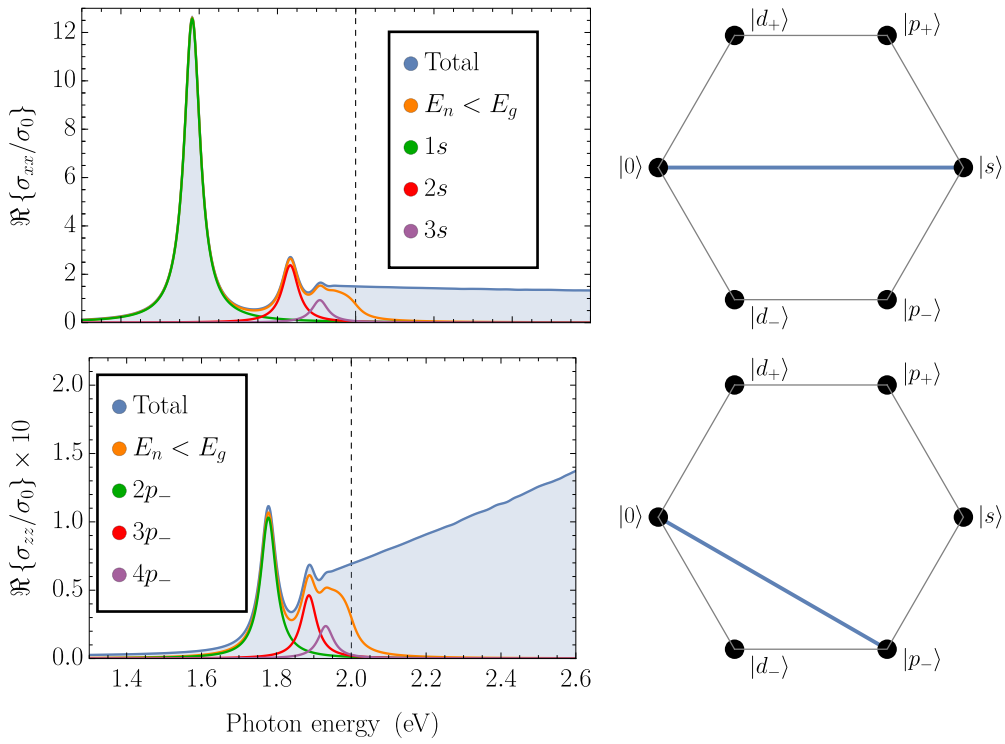

FIG. 2. (Left) Real part of the linear IP (top) and OOP (bottom) optical response for $\epsilon = 1$. The orange curve corresponds to the excitonic bound states, whereas the blue line also includes continuum states. The vertical dashed line represents the band gap. (Right) Diagram of dominant excitonic selection rules in the $\tau = 1$ valley for linear IP (top) and OOP (bottom) optical response.

momentum space by

$$E_n \psi^{(n)}_{cv\mathbf{k}} = E_{cv\mathbf{k}} \psi^{(n)}_{cv\mathbf{k}} + \sum_{\mathbf{q}} V(|\mathbf{k}-\mathbf{q}|)\langle c_{\mathbf{k}}|c_{\mathbf{q}}\rangle\langle v_{\mathbf{q}}|v_{\mathbf{k}}\rangle \psi^{(n)}_{cv\mathbf{q}}, \tag{16}$$

where E_n is the exciton energy of state n, $V(k)$ is the attractive electrostatic potential coupling electrons and holes, and $\psi^{(n)}_{cv\mathbf{k}}$ is the wave function of the exciton. In Eq. (16), the exchange term in the electrostatic potential has been ignored due to the weak effect on exciton binding energies [74,75]. Additionally, as we only consider exciton states with zero center-of-mass (COM) momentum (i.e., the zero-temperature limit), we will also ignore intervalley coupling phenomena [76]. For notational simplicity, the τ dependence of energy and wave function is omitted from the list of arguments. In Eq. (16), the valley dependence is present in the form factor $\langle c_{\mathbf{k}}|c_{\mathbf{q}}\rangle\langle v_{\mathbf{q}}|v_{\mathbf{k}}\rangle$. For our system, we consider $V(k)$ to be the Rytova-Keldysh potential [77,78], given in momentum space by

$$V(k) = -2\pi\hbar c\alpha \frac{1}{k(\epsilon + r_0 k)}, \tag{17}$$

with α the fine-structure constant, ϵ as the mean dielectric constant of the media surrounding the monolayer, and r_0 as an IP screening length [79] related to the polarizability of the material and usually obtained from density functional theory calculations [80]. From the analysis of Fig. 2(c) of Ref. [80] for graphenelike materials with a band gap of $E_g = 2$ eV, we set $r_0 = 40$ Å.

Considering the excitonic wave function to have a well-defined angular momentum ℓ_n, we write it as $\psi^{(n)}_{cv\mathbf{k}} = f^{(n)}_{cvk} e^{i\ell_n\theta_k}$ and, defining $\varphi = \theta_q - \theta_k$, rewrite the Bethe-Salpeter equation by converting the sum into an integral as

$$E_n f^{(n)}_{cvk} = 2\varepsilon f^{(n)}_{cvk} + \frac{1}{4\pi^2}\sum_{\lambda=0}^{2}\int_0^\infty\int_0^{2\pi} V(|\mathbf{k}-\mathbf{q}|)\mathcal{A}_\lambda(k,q) \times e^{i\lambda\tau\varphi} f^{(n)}_{cvq} e^{i\ell_n\varphi} d\varphi\, q dq, \tag{18}$$

where $E_{cv\mathbf{k}}$ became 2ε as we are neglecting the effects of trigonal warping on the band structure for simplicity. This approximation removes all coupling of states with different angular momentum, leading to selection rules identical to those of hBN and similar materials [59,65,66]. In principle, exchange corrections could also couple states with different angular momentum. However, following from Ref. [76], the lowest-order exchange correction at zero COM momentum will simply introduce a renormalization of the band gap, which will not couple different angular momentum state and, therefore, the optical selection rules remain unchanged.

The radial component of the form factor is obtained directly from the expansion of $\langle c_{\mathbf{k}}|c_{\mathbf{q}}\rangle\langle v_{\mathbf{q}}|v_{\mathbf{k}}\rangle$ whereas again neglecting trigonal warping in the definition of the eigenvectors. Under this approximation, the eigenvectors read

$$|v_{\mathbf{k}}\rangle = \begin{bmatrix} e^{-i\tau\theta}\sin\frac{x_k}{2} \\ \cos\frac{x_k}{2} \end{bmatrix}, \qquad |c_{\mathbf{k}}\rangle = \begin{bmatrix} -\cos\frac{x_k}{2} \\ e^{i\tau\theta}\sin\frac{x_k}{2} \end{bmatrix},$$

where $x_k = \tan^{-1}[\frac{\hbar v_F k}{\Delta}]$. The radial component of the form factor can then be written as

$$\mathcal{A}_\lambda(k,q) = \begin{cases} \frac{1}{4}(1+\cos x_k)(1+\cos x_q), & \lambda = 0, \\ \frac{1}{2}\sin x_k \sin x_q, & \lambda = 1, \\ \frac{1}{4}(1-\cos x_k)(1-\cos x_q), & \lambda = 2, \end{cases}$$

where λ denotes the angular dependence present in the $e^{i\lambda\tau\varphi}$ factor in Eq. (18).

As evident from Eq. (18), the degeneracy in angular momentum $\ell_n \leftrightarrow -\ell_n$ is immediately lifted within the same valley. However, a degeneracy between $(\ell_n + m_s, \tau)$ and $(-\ell_n - m_s, -\tau)$ excitons is still present, stemming from time-reversal symmetry in the system [81]. Finally, Eq. (18) is solved numerically via a simple numerical quadrature using a tangent grid $k = \tan(x\frac{\pi}{2})$ with 1000 points $x \in [0, 1]$, following the procedure already outlined several times in the literature, namely, in Refs. [63,82–84].

When discussing excitonic states, we will use nomenclature similar to the two-dimensional hydrogen atom to distinguish the different angular momentum states (i.e., s, $p_\pm$, and $d_\pm$ states). As the pseudospin contribution $m_s = 0$, s states will have $\ell = 0$, $p_\pm$ will have $\ell = \pm 1$, and analogous to higher angular momentum states.

IV. EXCITONIC OPTICAL RESPONSE

Having outlined the method for obtaining excitonic states in our system, we will now consider the excitonic optical conductivity. To extract the resonances, we add a broadening of $\hbar\Gamma = 0.05$ eV, introduced via the substitution $\hbar\omega \to \hbar\omega + i\frac{\hbar\Gamma}{2}$. Following Refs. [59,72,85,86], we define $\sigma_0 = \frac{e^2}{4\hbar}$ and write the linear conductivity as

$$\frac{\sigma_{\alpha\beta}(\omega)}{\sigma_0} = \frac{-i\hbar^2}{2\pi^3 m^2}\sum_n \left[\frac{E_n X^\alpha_{0n} X^\beta_{n0}}{E_n - \hbar\omega} - (\omega \to -\omega)^*\right]. \quad (19)$$

For the nonlinear conductivity, we are interested in both SC ($\omega_p = -\omega_q^*$) and SHG ($\omega_p = \omega_q$) regimes. Defining $\sigma_2 = \frac{e^3 a}{4E_g\hbar}$, we write the SHG nonlinear conductivity [59,72] as

$$\frac{\sigma^{\mathrm{SHG}}_{\alpha\beta\gamma}(\omega)}{\sigma_2} = \frac{-iE_g\hbar^2}{2a\pi^3 m^2}\sum_{n,m}\left[\frac{E_n X^\alpha_{0n} Q^\beta_{nm} X^\gamma_{m0}}{(E_n - 2\hbar\omega)(E_m - \hbar\omega)} - \frac{E_n X^\alpha_{n0} Q^\beta_{mn} X^\gamma_{0m}}{(E_n + 2\hbar\omega)(E_m + \hbar\omega)} - \frac{(E_n - E_m) X^\alpha_{0n} Q^\beta_{nm} X^\gamma_{m0}}{(E_n + \hbar\omega)(E_m - \hbar\omega)}\right]. \quad (20)$$

In these expressions, E_n is the energy of the excitonic state n, and the one- and two-state excitonic matrix elements are defined as [59,72]

$$X^\alpha_{0n} = i\int \psi^{(n)}_{cv\mathbf{k}} \frac{p^\alpha_{vc\mathbf{k}}}{E_{cv\mathbf{k}}} d^2\mathbf{k}, \quad (21)$$

and

$$Q^\alpha_{nm} = i\int \psi^{(n)*}_{cv\mathbf{k}} \left[\psi^{(m)}_{cv\mathbf{k}}\right]_{;k_\alpha} d^2\mathbf{k}, \quad (22)$$

where $[\psi^{(m)}_{cv\mathbf{k}}]_{;k_\alpha}$ is the generalized derivative [68] in the α direction of the exciton wave function for the state m given in terms of the Berry connection $\Omega^\alpha_{ij\mathbf{k}}$, defined as [72]

$$\left[\psi^{(m)}_{cv\mathbf{k}}\right]_{;k_\alpha} = \frac{\partial\psi^{(m)}_{cv\mathbf{k}}}{\partial k_\alpha} - i\left(\Omega^\alpha_{cc\mathbf{k}} - \Omega^\alpha_{vv\mathbf{k}}\right)\psi^{(m)}_{cv\mathbf{k}}. \quad (23)$$

Analogous to what was discussed regarding Eq. (15), the excitonic wave function will be independent of k_z and, as such, the $\frac{\partial}{\partial k_z}\psi^{(m)}_{cv\mathbf{k}}$ term is dropped, meaning that Q^z_{nm} reads

$$Q^z_{nm} = \int \psi^{(n)*}_{cv\mathbf{k}}\left(\Omega^z_{cc\mathbf{k}} - \Omega^z_{vv\mathbf{k}}\right)\psi^{(m)}_{cv\mathbf{k}} d^2\mathbf{k}. \quad (24)$$

Additionally, one can easily convert Eqs. (19) and (20) into formulas for the associated susceptibility as $\chi_{\alpha\beta} = \frac{i}{\omega\epsilon_0}\sigma_{\alpha\beta}$ and $\chi^{\mathrm{SHG}}_{\alpha\beta\gamma} = \frac{i}{2\omega\epsilon_0}\sigma^{\mathrm{SHG}}_{\alpha\beta\gamma}$, respectively [72].

V. OPTICAL RESPONSE OF BUCKLED GAPPED GRAPHENE

We will now quickly outline the IP optical selection rules for gapped graphene with trigonal warping, already discussed in the literature [59], before focusing our attention on the OOP linear and the nonlinear optical response of buckled gapped graphene.

As discussed in Sec. II, we will be ignoring $\pi - \sigma$ hybridization by assuming the buckling is much smaller than the lattice constant. Therefore, this model will be identical to the unbuckled monolayer discussed previously, apart from the alternating z positions of the individual sublattices. More importantly, the eigenstates will remain those given by Eqs. (7) and (8), meaning that no changes to either the momentum matrix elements or to the Bethe-Salpeter equation are needed.

Throughout, we will consider a buckling parameter $h = a/4$, where a is the lattice parameter. This matches approximately what is present in the literature [6,87–89] where, depending on the material in question, the buckling parameter h takes values between $a/2.5$ and $a/8.6$. Additionally, as will be evident, the presence of trigonal warping is not necessary to obtain finite linear and nonlinear OOP conductivities.

A. In-plane optical selection rules

To obtain the optical selection rules, we must compute the angular integrals present in the excitonic matrix elements X^x_{0n} and Q^x_{nm}. These optical selection rules are relevant not only for the IP linear and nonlinear responses, but also for the nondiagonal OOP response. For clarity, we separate this subsection into discussion on linear and nonlinear response. For the linear optical response, we focus on the angular integral present in the definition of X^x_{0n} following Eq. (21). To zeroth order in ζ_{TW}, the angular integral in Eq. (21) then reads

$$\int_0^{2\pi} e^{i\ell_n\theta} p^x_{vc\mathbf{k}} d\theta \propto \left[\frac{\Delta}{\varepsilon} + \frac{\ell_n + \tau}{|\ell_n + \tau|}\tau\right]\delta_{|\ell_n+\tau|,1}. \quad (25)$$

The presence of the Kronecker δ in Eq. (25) immediately gives rise to the well-known valley-dependent selection rules in gapped graphene, hexagonal boron nitride, and other monolayer materials with a hexagonal lattice [59,65,66,90,91] when one takes into account the valley-dependent pseudospin contribution. Including trigonal warping effects would lead to a quadratic correction allowing for transitions with $|\ell_n + \tau| = 2$ or $|\ell_n + \tau| = 4$.

For the nonlinear optical response, we first focus our attention on the angular integral in the definition of Q^x_{nm} following Eq. (22). Performing the necessary angular integral, we write the matrix elements in a somewhat abusive but concise form as

$$Q^x_{nm} = Q^x_{|\ell_{m,n}|=1} + \zeta_{\rm TW}\left[Q^x_{|\ell_{m,n}|=2} + Q^x_{|\ell_{m,n}|=4}\right], \tag{26}$$

where the new indices restrict each term to the Kronecker δ's resulting from the different angular integrals and we defined $\ell_{m,n} = \ell_m - \ell_n$ for conciseness. Besides the Q^x_{nm} matrix element, a linear contribution in $\zeta_{\rm TW}$ is also present in the expansion of X^x_{0n}. In the same notation, we write this contribution as

$$X^x_{0n} = X^x_{|\ell_n+\tau|=1} + \zeta_{\rm TW}\left[X^x_{|\ell_n+\tau|=2} + X^x_{|\ell_n+\tau|=4}\right]. \tag{27}$$

As we are considering contributions only up to first order in $\zeta_{\rm TW}$, we must carefully analyze the matrix product $X^x_{0n}Q^x_{nm}X^x_{m0}$ to understand which states are to be included. Knowing the simplified forms for the matrix elements, we can expand the oscillator strength $X^x_{0n}Q^x_{nm}X^x_{m0}$ up to linear order in $\zeta_{\rm TW}$. The nozero contributions to the nonlinear second-order conductivity then read

$$\begin{aligned}\zeta_{\rm TW}\Big[&X^x_{|\ell_n+\tau|=2}Q^x_{|\ell_{m,n}|=1}X^{x,*}_{|\ell_m+\tau|=1} + X^x_{|\ell_n+\tau|=1}Q^x_{|\ell_{m,n}|=2}X^{x,*}_{|\ell_m+\tau|=1}\\ &+ X^x_{|\ell_n+\tau|=1}Q^x_{|\ell_{m,n}|=1}X^{x,*}_{|\ell_m+\tau|=2}\Big],\end{aligned} \tag{28}$$

where the importance of including trigonal warping in order to obtain a nonzero second-order response is evident. Defining the oscillator strength $\sigma_{\ell_n;\ell_m} \equiv X^x_{\ell_n}Q^x_{\ell_n,\ell_m}X^x_{\ell_m}$ from the allowed transitions of Eq. (28), the dominant matrix elements correspond to the $\sigma_{p_+;s}$ and $\sigma_{s;p_+}$, in perfect agreement with Fig. 2(c) of Ref. [59].

B. Out-of-plane momentum and Berry connection

The matrix elements of z are given by $h\sigma_z$ with σ_z as the diagonal Pauli matrix and can be easily computed between bands n and m as

$$z_{nm\mathbf{k}} = \langle n_{\mathbf{k}}|\begin{bmatrix} h & 0 \\ 0 & -h\end{bmatrix}|m_{\mathbf{k}}\rangle \tag{29}$$

Under the same linear approximation in $\zeta_{\rm TW}$ for the band structure as discussed in Eq. (5) and considering only terms up to $O(\zeta^1_{\rm TW})$, Eq. (29) reads

$$z_{vc\mathbf{k}} = -he^{i\tau\theta}\sqrt{1-\frac{\Delta^2}{\varepsilon^2}}\left[1+\zeta_{\rm TW}\tau\frac{\Delta^2}{\varepsilon^2}ak\,\sin 3\theta\right], \tag{30}$$

$$\begin{aligned} z_{cc\mathbf{k}} &= h\frac{\Delta}{\varepsilon}\left[1-\zeta_{\rm TW}\tau\left(1-\frac{\Delta^2}{\varepsilon^2}\right)ak\,\sin 3\theta\right]\\ &= -z_{vv\mathbf{k}}\end{aligned} \tag{31}$$

for the different band pairs.

Knowing the $z_{ij\mathbf{k}}$ matrix elements, we can finally write the OOP component of the momentum and Berry connections as

$$\begin{aligned} p^z_{vc\mathbf{k}} &= \frac{m}{i\hbar}2\varepsilon z_{vc\mathbf{k}}\\ &= 2ih\frac{m}{\hbar}e^{i\tau\theta}\sqrt{\varepsilon^2-\Delta^2}\left[1+\zeta_{\rm TW}\tau\frac{\Delta^2}{\varepsilon^2}ak\,\sin 3\theta\right],\end{aligned} \tag{32}$$

and, following from [68]

$$\begin{aligned}\Omega^z_{cc\mathbf{k}} - \Omega^z_{vv\mathbf{k}} &= z_{cc\mathbf{k}} - z_{vv\mathbf{k}}\\ &= 2h\frac{\Delta}{\varepsilon}\left[1-\zeta_{\rm TW}ak\tau\left(1-\frac{\Delta^2}{\varepsilon^2}\right)\sin 3\theta\right].\end{aligned} \tag{33}$$

The jump from $\frac{\partial}{\partial k_z}$ to iz can be understood by considering the buckled monolayer as a repeated structure in the z direction. This means that the wave functions carry a $e^{ik_z z}$ factor, whereas the periodic parts [the eigenvectors in Eqs. (7) and (8)] are independent of k_z. Finally, the period of this repeated structure is taken to infinity.

Although the IP momentum in Eq. (25) goes to zero as $\Delta/\varepsilon \approx k^{-1}$ for large k, the dominant term of $p^z_{vc\mathbf{k}}$ is linear in k. As a consequence, contributions from continuum states (i.e., states where $E_n > 2\Delta$) will quickly increase with ω.

C. Out-of-plane excitonic linear conductivity

We will now analyze the OOP excitonic conductivity. Considering only the zeroth-order contribution from $\zeta_{\rm TW}$, it is immediately evident from the OOP momentum of Eq. (32) that only transitions to excitonic states with $\ell_n = -\tau$ are allowed, meaning that X^z_{0n} reads

$$X^z_{0n} = -\frac{2\pi hm}{\hbar}\delta_{\ell_n,-\tau}\int_0^\infty f^{(n)}_{cvk}\sqrt{1-\frac{\Delta^2}{\varepsilon^2}}k\,dk. \tag{34}$$

Including trigonal warping effects would allow for transitions where $|\ell_n + \tau| = 3$ and the correction would be quadratic in $\zeta_{\rm TW}$.

The real part of the linear excitonic optical conductivity of the buckled monolayer for $\epsilon = 1$ is plotted in Fig. 2 with the top panel as the IP response, and the bottom panel as the OOP response. Right side diagrams represent the transitions allowed for each component in the $\tau = 1$ valley. Considering the $\tau = -1$ valley would imply a sign flip of the diagrams (e.g., exchanging p_- by p_+, etc.), as evident from the selection rules of Eqs. (27) and (34). As expected from the form of the momentum operator p^z_{vc}, we observe an ever-increasing linear optical conductivity when accounting for continuum states (see Appendix B) as well as direct proportionality to $(h/a)^2$. The optical response present in the bottom panel of Fig. 2 also qualitatively matches the measured optical conductivity of anisotropic materials, such as ZrSiS, ZrGeS, and ZrGeSe, found in the current literature [15,18].

D. Out-of-plane excitonic nonlinear conductivity

Focusing now on the nonlinear regime and considering only zeroth order in $\zeta_{\rm TW}$ contributions, the Q^z_{nm} matrix

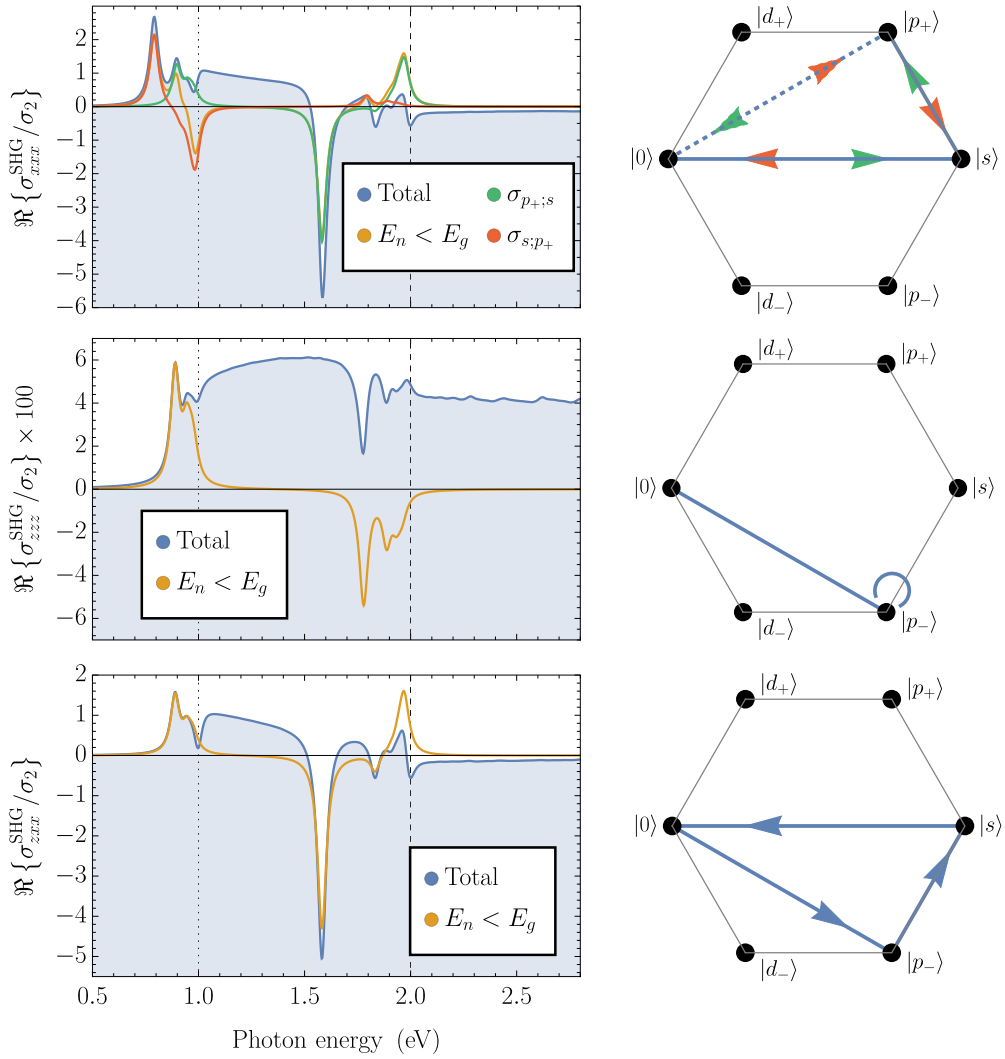

FIG. 3. (Left) Real part of the SHG optical response with diagonal IP (top), diagonal OOP (middle) and nondiagonal OOP (bottom) conductivity for $\epsilon = 1$, $h = a/4$. The orange curve corresponds to only excitonic bound states, whereas blue line also includes continuum states. The vertical (dotted) dashed black lines represent (half) the band gap of the system. (Right) Diagram of dominant excitonic selection rules in the $\tau = 1$ valley for each component. The dashed line means the transition is allowed by trigonal warping, and thesolid lines are transitions allowed without trigonal warping. Arrow direction and color represent the specific resonance when multiple contributions are present.

element reads

$$Q^z_{nm} = 4\pi h \delta_{\ell_m,\ell_n} \int_0^\infty f^{(n)*}_{cvk} \frac{\Delta}{\varepsilon} f^{(m)}_{cvk} k\, dk, \tag{35}$$

allowing transitions between states with the same angular momentum. However, as X^z_{0n} only allows $\ell_n = -\tau$ to zeroth order in $\zeta_{\rm TW}$, we arrive at the fact that only $\ell_n = \ell_m = -1$ states contribute in the $\tau = 1$ valley.

Including trigonal warping effects in Q^z_{nm} would allow for transitions where $|\ell_m - \ell_n| = 3$. Considering this extra term together with the selection rules present in X^z_{0n} leads to a vanishing first-order contribution from $\zeta_{\rm TW}$ to the nonlinear conductivity. As each momentum matrix element will carry a factor of h as clear from Eqs. (34) and (35), and working in the present approximation where the hopping γ is independent of h, the nonlinear conductivity will be strictly cubic in h/a. The SHG conductivity is plotted in the middle panel of Fig. 3 for $\epsilon = 1$. Apart from the much smaller amplitude due to the cubic dependence on h/a, it is also noteworthy that the response above $\hbar\omega = 2$ eV remains remarkably close to its maximum value. This is very different from what occurs for the IP response where the response above $\hbar\omega = 2$ eV is much smaller than its maximum value.

E. Nondiagonal out-of-plane response

Finally, we will consider the nondiagonal OOP response in buckled gapped graphene. Considering again only the x direction for the IP response, we have three different components, which can prove interesting: σ_{zxx}, σ_{xzx}, and σ_{zzx}.

Looking more carefully at the selection rules of the system, we can immediately tell that $\sigma_{zzx} = 0$ when recalling Eqs. (27), (34), and (35): whereas, X^z_{0n} and Q^z_{nm} only allow $\ell_n = \ell_m = -1$ states, X^x_{0n} explicitly forbids these states. As such, we focus our attention only on σ_{zxx}. Although we will not be discussing σ_{xzx}, a quick analysis of the various

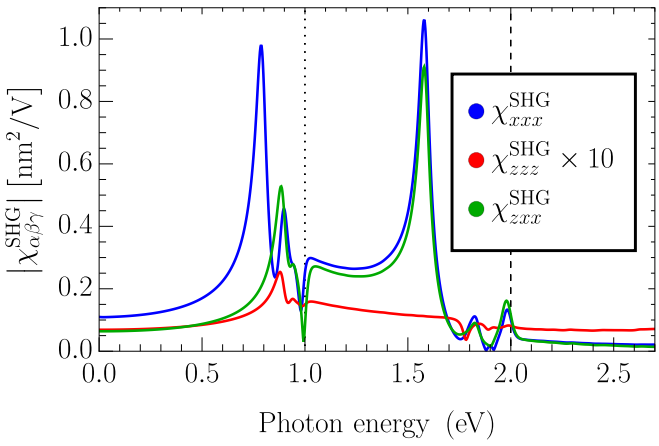

FIG. 4. Magnitude of three different components (xxx, zzz, and zxx) of SHG nonlinear optical susceptibilities for $\epsilon = 1$, $h = a/4$. The vertical (dotted) dashed black lines represent (half) the band gap of the system.

selection rules discussed previously shows that the dominant response will be a zeroth-order contribution in $\zeta_{\rm TW}$ of the form $X^x_{\ell_n=0} Q^z_{nm} X^x_{\ell_m=0}$. Under Kleinman symmetry [92], σ_{xzx} will be approximately equal to σ_{zxx}.

Now, explicitly computing the selection rules for σ_{zxx}, X^z_{0n} again immediately forces $\ell_n = -1$. Recalling Eqs. (26) and (27), the dominant transition will be associated with the matrix elements $Q^x_{|\ell_{m,n}|=1} X^x_{|\ell_m+\tau|=1}$ (i.e., zeroth-order contribution in $\zeta_{\rm TW}$), meaning that ℓ_m is restricted to $|\ell_m + \tau| = 1$. Excluding all other contributions, we can immediately expect that this off-diagonal term will be significantly larger than $\sigma^{(2)}_{zzz}$ as the dependence on $h/a < 1$ will be linear instead of cubic. Additionally, X^x_{m0} is much larger than X^z_{m0}, which will also contribute to this trend.

This excitonic nonlinear conductivity is then plotted in the bottom panel of Fig. 3 for $\epsilon = 1$. As expected from the qualitative analysis of the matrix elements, the relative magnitude of the off-diagonal OOP contribution is much larger than the diagonal OOP response present in the top panel of Fig. 3. As discussed previously, this mainly stems from the lower-order dependence in h/a (linear instead of cubic). Additionally, and as expected from the general form σ_{zxx}, we can also observe that the bound state peaks corresponding to $2\hbar\omega = E_n$ (i.e., states below $\hbar\omega = \Delta$) match exactly with the corresponding regime in σ_{zzz}, whereas, those corresponding to $\hbar\omega = E_m$ match exactly with the same regime in σ_{xxx}.

We also observe that the magnitude of $\sigma^{\rm SHG}_{zxx}$ is remarkably close to that of $\sigma^{\rm SHG}_{xxx}$ for the buckling parameter chosen. This will, of course, be dictated by the ratio h/a, meaning that for a larger buckling parameter the nondiagonal OOP SHG response will be larger than the diagonal IP SHG response. Additionally, in Appendix A, we plot the SC for the three different tensor elements discussed previously.

Finally, we present the xxx, zzz, and zxx components of the absolute value of the SHG nonlinear optical susceptibilities. These can be directly computed from the conductivity as

$$\chi^{\rm SHG}_{\alpha\beta\gamma} = \frac{i}{2\omega\epsilon_0} \sigma^{\rm SHG}_{\alpha\beta\gamma}, \tag{36}$$

and their absolute value is presented in Fig. 4. Due to the inclusion of a finite broadening $\hbar\Gamma = 0.05$ eV, the three considered tensor elements of the conductivity take a small but nonzero value at $\hbar\omega = 0$ with its magnitude less than 1% of the maximum of each tensor component. Still, the presence of this finite value at $\hbar\omega = 0$ means that the broadening must also be considered in the $1/\omega$ factor present in Eq. (36).

The relative amplitudes of the different components can be easily compared with χ_{zxx} presenting a very similar amplitude to χ_{xxx}. Additionally, χ_{zzz} is roughly a factor of $1/20$ smaller than either χ_{xxx} or χ_{zxx} within the band gap of the system as expected from the cubic dependence on the ratio h/a. The different dependence on h/a in each component means that as discussed previously choosing a larger buckling parameter will lead to a comparatively greater OOP susceptibility. Notably, the left-most peak of χ_{xxx} is not present in χ_{zxx}. This is due to the different selection rules for the two components of the SHG nonlinear susceptibility where certain transitions present in χ_{xxx} are no longer allowed for χ_{zxx}.

VI. SUMMARY

In this paper, we studied the excitonic linear and nonlinear optical properties of anisotropic-buckled monolayer semiconductors. To this end, we began by considering the gapped Dirac model with trigonal warping. The excitonic states were computed by numerical diagonalization of the Bethe-Salpeter equation, allowing us to explicitly discuss the excitonic selection rules of the system.

Introducing a small buckling in the lattice structure of the monolayer, we then obtained the OOP momentum matrix elements and Berry connections, discussing the resulting OOP excitonic optical selection rules. We then analyzed the xxx, zzz, and zxx tensor elements of both SHG and SC optical response, discussing the differences and similarities between the three components.

Finally, we computed the absolute value of the nonlinear optical susceptibility, directly comparing the amplitudes of the χ_{xxx}, χ_{zzz}, and χ_{zxx} matrix elements. The OOP magnitudes are, of course, dictated by the ratio between the buckling parameter (h) and the lattice constant (a), meaning that a structure with a different buckling parameter will present greatly different relative magnitudes. Although the OOP diagonal component had a much smaller maximum amplitude, stemming from the cubic dependence on the ratio h/a, the nondiagonal OOP component had a very similar amplitude to that of the diagonal IP component.

ACKNOWLEDGMENT

M.F.C.M.Q. acknowledges the International Iberian Nanotechnology Laboratory (INL) and the Portuguese Foundation for Science and Technology (FCT) for the Quantum Portugal Initiative (QPI) Grant No. SFRH/BD/151114/2021.

APPENDIX A: SHIFT-CURRENT NONLINEAR EXCITONIC CONDUCTIVITY

In this Appendix, we present plots of the SC for the xxx, zzz, and zxx tensor elements of the excitonic nonlinear

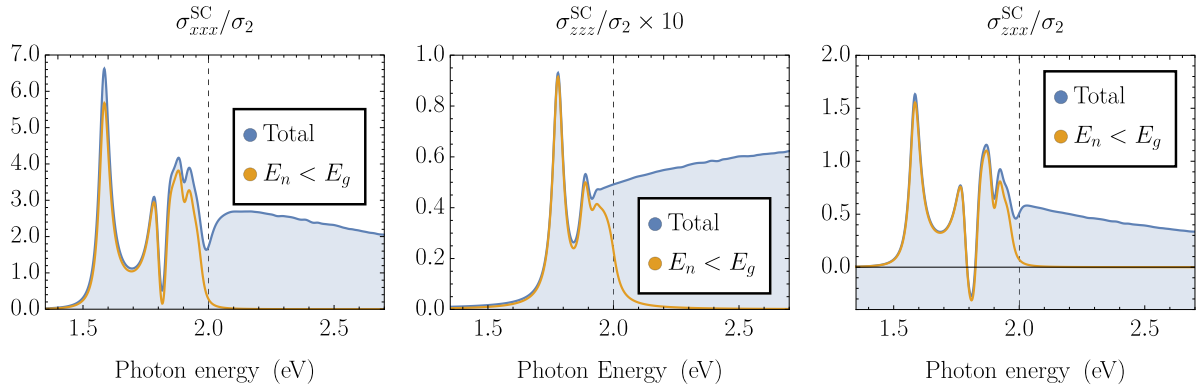

FIG. 5. Nonlinear SC IP (top), diagonal OOP (middle), and nondiagonal OOP (bottom) optical for $\epsilon = 1$, $h = a/4$. The orange curve corresponds to only excitonic bound states, whereas, the blue line also includes continuum states. The vertical dashed black lines represent the band gap of the system.

conductivity. As the selection rules are the same as presented in Fig. 3, they are not included in the SC plots of Fig. 5.

APPENDIX B: ELECTRONIC LINEAR AND NONLINEAR CONDUCTIVITY EXPRESSIONS

In this Appendix, we will present the expressions for the free-carrier conductivity in our monolayer system. These were computed directly from the definitions in Eqs. (13) and (14) whereas, considering only contributions up to first order in ζ_{TW}. For this effect, we recall the definitions of the in- and OOP momentum matrix elements and Berry connections from Ref. [59] (with the appropriate gauge transformation) and Eqs. (32) and (33).

In the following expressions $E_{cv\mathbf{k}} = E_{cvk}$ as including the contribution from trigonal warping in the band structure would introduce contributions one order higher in ζ_{TW}, which would then vanish upon integration and summation over valley. As such, the band structure now only depends on the radial component k, meaning that $E_{cvk} = 2\varepsilon$, where ε is as defined in Eq. (6). As an example, the nonlinear IP response would, up to first order, include an extra term originating from $p^{\alpha}_{vc\mathbf{k}}[p^{\beta}_{cv\mathbf{k}}]_{;k_\lambda}$ expanded to zeroth order, which vanishes upon integration.

Starting with the diagonal linear response described in Eq. (13), it follows that

$$\frac{\sigma_{xx}(\omega)}{\sigma_0} = \frac{2i}{\pi}\left[\frac{E_g}{\hbar\omega} - \left(1 + \frac{E_g^2}{\hbar^2\omega^2}\right)\tanh^{-1}\left(\frac{\hbar\omega}{E_g}\right)\right], \quad \text{(B1)}$$

where $E_g = 2\Delta$ and $\tanh^{-1}$ is the inverse hyperbolic tangent.

Under a similar analysis, we compute the angular integral present in Eq. (14) and obtain the generic radial integral form

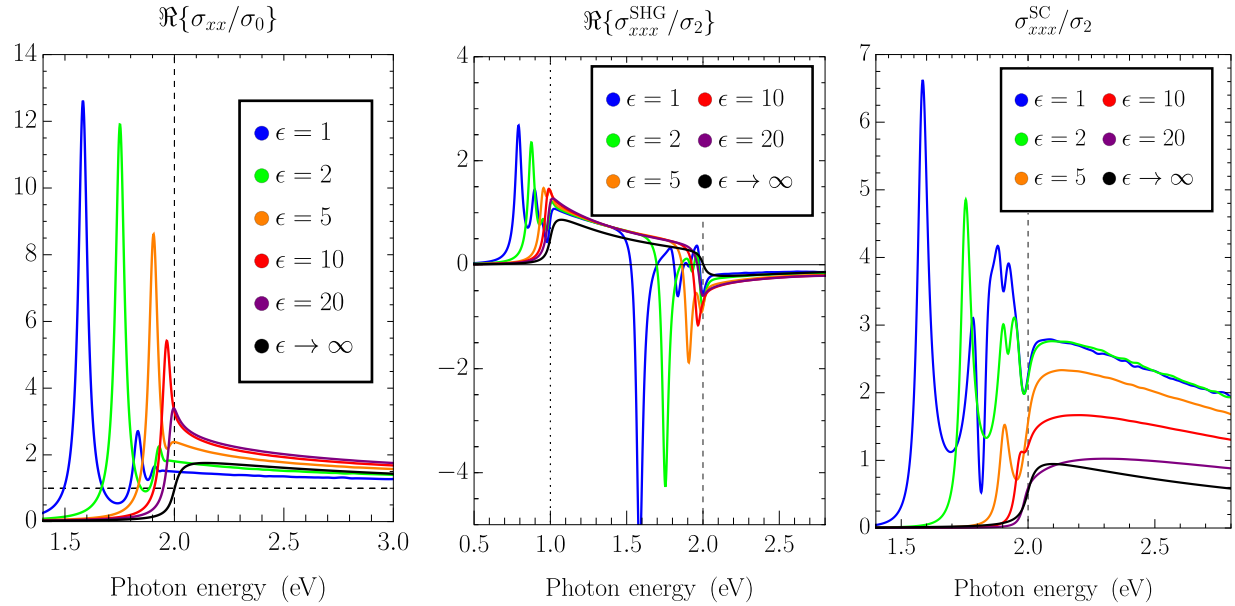

FIG. 6. Convergence of the real part of the (left) linear, (middle) SHG, and (right) SC IP optical response towards the free-carrier limit as the dielectric constant ϵ increases. The vertical axis is in units of σ_0 for the linear response and σ_2 for the nonlinear response.

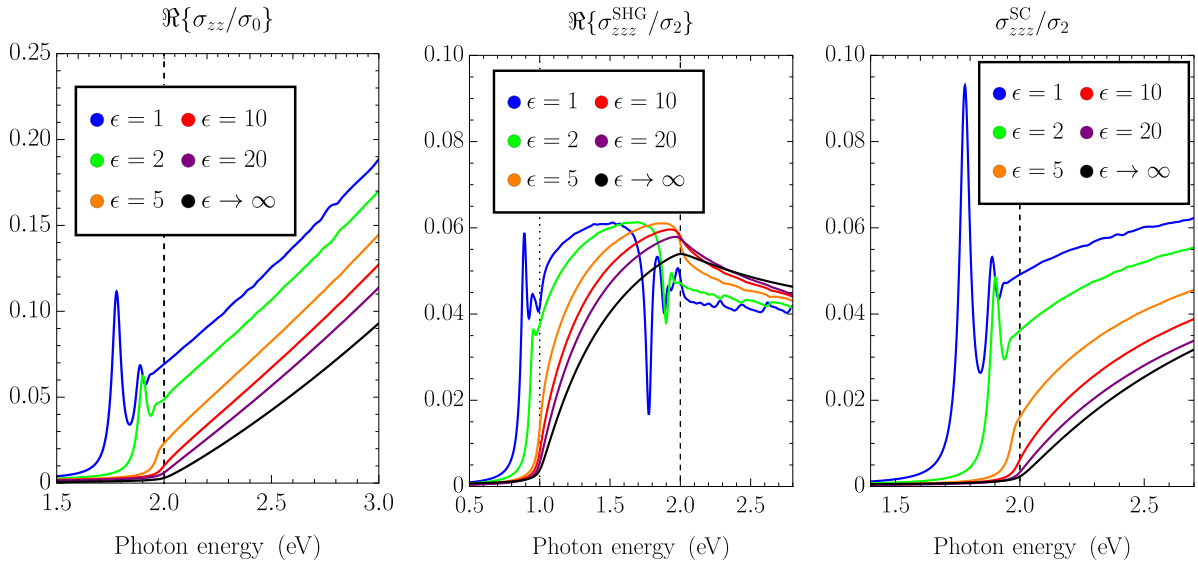

FIG. 7. Same as Fig. 6 except for the diagonal OOP response.

of the diagonal second-order response as

$$\frac{\sigma^{(\rm intra)}_{xxx}(\omega_p,\omega_q)}{\sigma_2} = i\frac{4\zeta_{\rm TW}}{\pi}E_g^2\int_{E_g}^{\infty}\frac{\hbar\omega_p+\hbar\omega_{pq}}{\left(E_{cvk}^2-\hbar^2\omega_q^2\right)\left(E_{cvk}^2-\hbar^2\omega_{pq}^2\right)} \times dE_{cvk} + (p\leftrightarrow q). \tag{B2}$$

Choosing specifically SHG and SC processes, we obtain

$$\frac{\sigma^{\rm SHG}_{xxx}(\omega)}{\sigma_2} \equiv \frac{\sigma^{(\rm intra)}_{xxx}(\omega,\omega)}{\sigma_2} = i\frac{8\zeta_{\rm TW}}{\pi}\left(\frac{E_g}{\hbar\omega}\right)^2\left[\tanh^{-1}\left(\frac{\hbar\omega}{E_g}\right) - \frac{1}{2}\tanh^{-1}\left(\frac{2\hbar\omega}{E_g}\right)\right], \tag{B3}$$

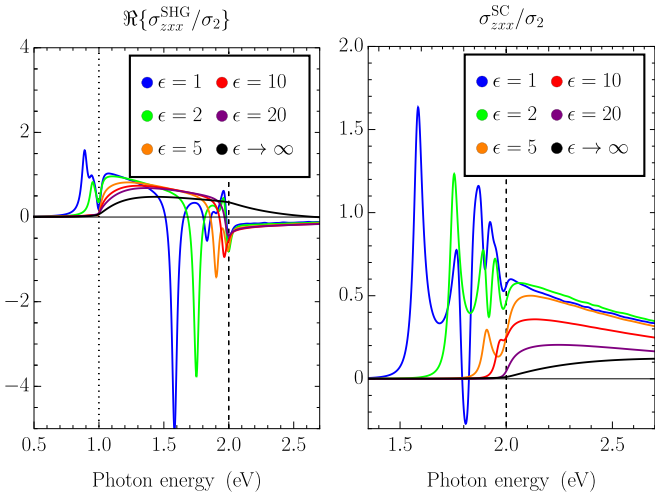

FIG. 8. Convergence of the real part of the off-diagonal OOP SHG (left) and SC (right) zxx optical response towards the free-carrier limit as the dielectric constant ϵ increases. The vertical axis is in units of σ_2.

and

$$\frac{\sigma^{\rm SC}_{xxx}(\omega)}{\sigma_2} \equiv \frac{\sigma^{(\rm intra)}_{xxx}(\omega,-\omega^*)}{\sigma_2} = \frac{16\zeta_{\rm TW}}{\pi}{\rm Im}\left[\left(\frac{E_g}{\hbar\omega}\right)^2\tanh^{-1}\left(\frac{\hbar\omega}{E_g}\right) - \frac{E_g}{\hbar\omega}\right], \tag{B4}$$

where Im denotes the imaginary part.

A similar analysis can be performed for the diagonal OOP linear and nonlinear response, although one must compute σ_{zz} carefully as the integration leads to a divergent result if the infinite k space is considered. This is, however, only true for the imaginary part. Restricting our analysis to the real part, we find a finite result reading

$${\rm Re}\left[\frac{\sigma_{zz}(\omega)}{\sigma_0}\right] \approx \frac{8}{3\gamma^2}\left(\frac{h}{a}\right)^2\left(\hbar^2\omega^2 - E_g^2\right)H(\hbar\omega - E_g), \tag{B5}$$

where $H(x)$ represents the Heaviside step function. For the diagonal nonlinear response, no convergence issues are present, and the integral can be considered over the infinite k space,

$$\frac{\sigma^{(\rm intra)}_{zzz}(\omega_p,\omega_q)}{\sigma_2} = \frac{32\hbar(\omega_p+\omega_{pq})E_g^2}{3i\pi\gamma^2}\left(\frac{h}{a}\right)^3 \times \int_{E_g}^{\infty}\frac{E_{cvk}^2 - E_g^2}{\left(E_{cvk}^2-\hbar^2\omega_p^2\right)\left(E_{cvk}^2-\hbar^2\omega_{pq}^2\right)} \times dE_{cvk} + (p\leftrightarrow q). \tag{B6}$$

Again restricting our analysis to SHG and SC, we obtain

$$\frac{\sigma^{\rm SHG}_{zzz}(\omega)}{\sigma_2} = \frac{32E_g^2}{3i\pi\gamma^2}\left(\frac{h}{a}\right)^3\left[\left(\frac{E_g^2}{\hbar^2\omega^2}-1\right)\tanh^{-1}\left(\frac{\hbar\omega}{E_g}\right) - \frac{1}{2}\left(\frac{E_g^2}{\hbar^2\omega^2}-4\right)\tanh^{-1}\left(\frac{2\hbar\omega}{E_g}\right)\right] \tag{B7}$$

and

$$\frac{\sigma_{zzz}^{\mathrm{SC}}(\omega)}{\sigma_2} = \frac{32E_g^2}{\pi\gamma^2}\left(\frac{h}{a}\right)^3 \mathrm{Im}\left[\frac{E_g}{\hbar\omega} + \left(1 - \frac{E_g^2}{\hbar^2\omega^2}\right)\tanh^{-1}\left(\frac{\hbar\omega}{E_g}\right)\right]. \tag{B8}$$

Finally, we consider the off-diagonal OOP response σ_{zxx}, where we can also consider the integral over infinite $k$space, reading

$$\frac{\sigma_{zxx}^{(\mathrm{intra})}(\omega_p,\omega_q)}{\sigma_2} = 16i\frac{(\hbar\omega_p + \hbar\omega_{pq})}{\pi}\Delta^2\frac{h}{a} \times \int_{E_g}^{\infty} \frac{E_g^2 - E_{cvk}^2}{E_{cvk}^2\left(E_{cvk}^2 - \hbar^2\omega_q^2\right)\left(E_{cvk}^2 - \hbar^2\omega_{pq}^2\right)} dE_{cvk} + (p \leftrightarrow q). \tag{B9}$$

Looking again at SHG and SC, we obtain

$$\frac{\sigma_{zxx}^{\mathrm{SHG}}(\omega)}{\sigma_2} = i\frac{1}{\pi}\frac{h}{a}\frac{E_g^2}{\hbar^2\omega^2}\left[3\frac{E_g}{\hbar\omega} - 2\left(\frac{E_g^2}{\hbar^2\omega^2} - 1\right)\tanh^{-1}\left(\frac{\hbar\omega}{E_g}\right) + \frac{1}{2}\left(\frac{E_g^2}{\hbar^2\omega^2} - 4\right)\tanh^{-1}\left(\frac{2\hbar\omega}{E_g}\right)\right] \tag{B10}$$

and

$$\frac{\sigma_{zxx}^{\mathrm{SC}}(\omega)}{\sigma_2} = \frac{4}{\pi}\frac{h}{a}\mathrm{Im}\left[\frac{E_g^3}{\hbar^3\omega^3} - \frac{2E_g}{3\hbar\omega} + \frac{E_g^2}{\hbar^2\omega^2}\left(1 - \frac{E_g^2}{\hbar^2\omega^2}\right)\tanh^{-1}\left(\frac{\hbar\omega}{E_g}\right)\right]. \tag{B11}$$

Knowing these expressions, we can study the convergence of the excitonic conductivities towards the free-carrier regime as the dielectric constant increases. This is plotted in Figs. 6–8 for dielectric constant ϵ between 1 and 20 as well as the free-carrier limit (in black). In these plots, we can see the excitonic conductivity converging towards the free-carrier regime as the dielectric constant of the medium surrounding the monolayer increases as expected from the fast drop of binding energies and number of bound states.

[1] A.-Y. Lu, H. Zhu, J. Xiao, C.-P. Chuu, Y. Han, M.-H. Chiu, C.-C. Cheng, C.-W. Yang, K.-H. Wei, Y. Yang, Y. Wang, D. Sokaras, D. Nordlund, P. Yang, D. A. Muller, M.-Y. Chou, X. Zhang, and L.-J. Li, Janus monolayers of transition metal dichalcogenides, Nat. Nanotechnol. **12**, 744 (2017).

[2] J. Zhang, S. Jia, I. Kholmanov, L. Dong, D. Er, W. Chen, H. Guo, Z. Jin, V. B. Shenoy, L. Shi, and J. Lou, Janus monolayer transition-metal dichalcogenides, ACS Nano **11**, 8192 (2017).

[3] T. Zheng, Y.-C. Lin, Y. Yu, P. Valencia-Acuna, A. A. Puretzky, R. Torsi, C. Liu, I. N. Ivanov, G. Duscher, D. B. Geohegan, Z. Ni, K. Xiao, and H. Zhao, Excitonic dynamics in janus MoSSe and WSSe monolayers, Nano Lett. **21**, 931 (2021).

[4] H. Şahin, S. Cahangirov, M. Topsakal, E. Bekaroglu, E. Akturk, R. T. Senger, and S. Ciraci, Monolayer honeycomb structures of group-IV elements and III-V binary compounds: First-principles calculations, Phys. Rev. B **80**, 155453 (2009).

[5] H. K. Avetissian and G. F. Mkrtchian, Higher harmonic generation by massive carriers in buckled two-dimensional hexagonal nanostructures, Phys. Rev. B **99**, 085432 (2019).

[6] M.-Q. Le, H.-T. Nguyen, and T.-L. Bui, Fracture of 28 buckled two-dimensional hexagonal sheets, Mech. Adv. Mater. Struct. **29**, 4993 (2022).

[7] R. Y. Kezerashvili and A. Spiridonova, Effects of parallel electric and magnetic fields on Rydberg excitons in buckled two-dimensional materials, Phys. Rev. B **103**, 165410 (2021).

[8] C.-H. Park and S. G. Louie, Tunable excitons in biased bilayer graphene, Nano Lett. **10**, 426 (2010).

[9] Y. Gong, J. Lin, X. Wang, G. Shi, S. Lei, Z. Lin, X. Zou, G. Ye, R. Vajtai, B. I. Yakobson, H. Terrones, M. Terrones, B.-K. Tay, J. Lou, S. T. Pantelides, Z. Liu, W. Zhou, and P. M. Ajayan, Vertical and in-plane heterostructures from WS_2/MoS_2 monolayers, Nat. Mater. **13**, 1135 (2014).

[10] P. Rivera, K. L. Seyler, H. Yu, J. R. Schaibley, J. Yan, D. G. Mandrus, W. Yao, and X. Xu, Valley-polarized exciton dynamics in a 2D semiconductor heterostructure, Science **351**, 688 (2016).

[11] S. J. Brun and T. G. Pedersen, Intense and tunable second-harmonic generation in biased bilayer graphene, Phys. Rev. B **91**, 205405 (2015).

[12] G. Antonius, D. Y. Qiu, and S. G. Louie, Orbital symmetry and the optical response of single-layer MX monochalcogenides, Nano Lett. **18**, 1925 (2018).

[13] S. Niu, G. Joe, H. Zhao, Y. Zhou, T. Orvis, H. Huyan, J. Salman, K. Mahalingam, B. Urwin, J. Wu, Y. Liu, T. E. Tiwald, S. B. Cronin, B. M. Howe, M. Mecklenburg, R. Haiges, D. J. Singh, H. Wang, M. A. Kats, and J. Ravichandran, Giant optical anisotropy in a quasi-one-dimensional crystal, Nat. Photon. **12**, 392 (2018).

[14] M. Brotons-Gisbert, R. Proux, R. Picard, D. Andres-Penares, A. Branny, A. Molina-Sánchez, J. F. Sánchez-Royo, and B. D. Gerardot, Out-of-plane orientation of luminescent excitons in two-dimensional indium selenide, Nat. Commun. **10**, 3913 (2019).

[15] J. Ebad-Allah, S. Rojewski, M. Vöst, G. Eickerling, W. Scherer, E. Uykur, R. Sankar, L. Varrassi, C. Franchini, K.-H. Ahn, J. Kuneš, and C. A. Kuntscher, Pressure-Induced Excitations in the Out-of-Plane Optical Response of the Nodal-Line Semimetal ZrSiS, Phys. Rev. Lett. **127**, 076402 (2021).

[16] G. A. Ermolaev, D. V. Grudinin, Y. V. Stebunov, K. V. Voronin, V. G. Kravets, J. Duan, A. B. Mazitov, G. I. Tselikov, A. Bylinkin, D. I. Yakubovsky, S. M. Novikov, D. G. Baranov, A. Y. Nikitin, I. A. Kruglov, T. Shegai, P. Alonso-González, A. N. Grigorenko, A. V. Arsenin, K. S. Novoselov, and V. S.

Volkov, Giant optical anisotropy in transition metal dichalcogenides for next-generation photonics, Nat. Commun. **12**, 854 (2021).

[17] X. Yang, P. Yang, X. Zhou, W. Feng, and Y. Yao, First- and second-order magneto-optical effects and intrinsically anomalous transport in the two-dimensional van der Waals layered magnets Crxy(x = S, Se, Te; y = Cl, Br, I), Phys. Rev. B **106**, 054408 (2022).

[18] J. Ebad-Allah, S. Rojewski, Y. L. Zhu, Z. Q. Mao, and C. A. Kuntscher, In-plane and out-of-plane optical response of the nodal-line semimetals ZrGeS and ZrGeSe, Phys. Rev. B **106**, 075143 (2022).

[19] M. M. Petrić, V. Villafañe, P. Herrmann, A. B. Mhenni, Y. Qin, Y. Sayyad, Y. Shen, S. Tongay, K. Müller, G. Soavi, J. J. Finley, and M. Barbone, Nonlinear dispersion relation and out-of-plane second harmonic generation in MoSSe and WSSe janus monolayers, arXiv:2303.03844.

[20] J. Shi, H. Xu, C. Heide, C. HuangFu, C. Xia, F. de Quesada, H. Shen, T. Zhang, L. Yu, A. Johnson, F. Liu, E. Shi, L. Jiao, T. Heinz, S. Ghimire, J. Li, J. Kong, Y. Guo, and A. M. Lindenberg, Giant room-temperature nonlinearities from a monolayer janus topological semiconductor, arXiv:2304.00750.

[21] Y. Wei, X. Xu, S. Wang, W. Li, and Y. Jiang, Second harmonic generation in janus MoSSe a monolayer and stacked bulk with vertical asymmetry, Phys. Chem. Chem. Phys. **21**, 21022 (2019).

[22] A. Strasser, H. Wang, and X. Qian, Nonlinear optical and photocurrent responses in janus MoSSe monolayer and MoS_2–MoSSe van der Waals heterostructure, Nano Lett. **22**, 4145 (2022).

[23] N. A. Pike and R. Pachter, Angular dependence of the second-order nonlinear optical response in janus transition metal dichalcogenide monolayers, J. Phys. Chem. C **126**, 16243 (2022).

[24] M.-E. Kleemann, R. Chikkaraddy, E. M. Alexeev, D. Kos, C. Carnegie, W. Deacon, A. C. de Pury, C. Große, B. de Nijs, J. Mertens, A. I. Tartakovskii, and J. J. Baumberg, Strong-coupling of WSe_2 in ultra-compact plasmonic nanocavities at room temperature, Nat. Commun. **8**, 1296 (2017).

[25] M. Stührenberg, B. Munkhbat, D. G. Baranov, J. Cuadra, A. B. Yankovich, T. J. Antosiewicz, E. Olsson, and T. Shegai, Strong light–matter coupling between plasmons in individual gold bi-pyramids and excitons in mono- and multilayer WSe_2, Nano Lett. **18**, 5938 (2018).

[26] O. Dogadov, C. Trovatello, B. Yao, G. Soavi, and G. Cerullo, Parametric nonlinear optics with layered materials and related heterostructures, Laser Photon. Rev. **16**, 2100726 (2022).

[27] Y. Zhang, Y. Wang, Y. Dai, X. Bai, X. Hu, L. Du, H. Hu, X. Yang, D. Li, Q. Dai, T. Hasan, and Z. Sun, Chirality logic gates, Sci. Adv. **8**, eabq8246 (2022).

[28] Y. Li, N. An, Z. Lu, Y. Wang, B. Chang, T. Tan, X. Guo, X. Xu, J. He, H. Xia, Z. Wu, Y. Su, Y. Liu, Y. Rao, G. Soavi, and B. Yao, Nonlinear co-generation of graphene plasmons for optoelectronic logic operations, Nat. Commun. **13**, 3138 (2022).

[29] A. Dasgupta, J. Gao, and X. Yang, Atomically thin nonlinear transition metal dichalcogenide holograms, Nano Lett. **19**, 6511 (2019).

[30] G. Soavi, G. Wang, H. Rostami, D. G. Purdie, D. De Fazio, T. Ma, B. Luo, J. Wang, A. K. Ott, D. Yoon, S. A. Bourelle, J. E. Muench, I. Goykhman, S. Dal Conte, M. Celebrano, A. Tomadin, M. Polini, G. Cerullo, and A. C. Ferrari, Broadband, electrically tunable third-harmonic generation in graphene, Nat. Nanotechnol. **13**, 583 (2018).

[31] S. Klimmer, O. Ghaebi, Z. Gan, A. George, A. Turchanin, G. Cerullo, and G. Soavi, All-optical polarization and amplitude modulation of second-harmonic generation in atomically thin semiconductors, Nat. Photon. **15**, 837 (2021).

[32] K. Takeda and K. Shiraishi, Theoretical possibility of stage corrugation in Si and Ge analogs of graphite, Phys. Rev. B **50**, 14916 (1994).

[33] Z. Zhu and D. Tománek, Semiconducting Layered Blue Phosphorus: A Computational Study, Phys. Rev. Lett. **112**, 176802 (2014).

[34] S. Zhang, Z. Yan, Y. Li, Z. Chen, and H. Zeng, Atomically thin arsenene and antimonene: Semimetal–semiconductor and indirect–direct band-gap transitions, Angew. Chem. Int. Ed. **54**, 3112 (2015).

[35] C. Kamal and M. Ezawa, Arsenene: Two-dimensional buckled and puckered honeycomb arsenic systems, Phys. Rev. B **91**, 085423 (2015).

[36] G. Wang, R. Pandey, and S. P. Karna, Atomically thin group V elemental films: Theoretical investigations of antimonene allotropes, ACS Appl. Mater. Interfaces **7**, 11490 (2015).

[37] S. Zhang, M. Xie, F. Li, Z. Yan, Y. Li, E. Kan, W. Liu, Z. Chen, and H. Zeng, Semiconducting group 15 monolayers: A broad range of band gaps and high carrier mobilities, Angew. Chem., Int. Ed. **55**, 1666 (2016).

[38] C. Kamal, A. Chakrabarti, and M. Ezawa, Direct band gaps in group IV-VI monolayer materials: Binary counterparts of phosphorene, Phys. Rev. B **93**, 125428 (2016).

[39] J.-A. Yan, S.-P. Gao, R. Stein, and G. Coard, Tuning the electronic structure of silicene and germanene by biaxial strain and electric field, Phys. Rev. B **91**, 245403 (2015).

[40] A. Molle, J. Goldberger, M. Houssa, Y. Xu, S.-C. Zhang, and D. Akinwande, Buckled two-dimensional Xene sheets, Nat. Mater. **16**, 163 (2017).

[41] Z. Ni, Q. Liu, K. Tang, J. Zheng, J. Zhou, R. Qin, Z. Gao, D. Yu, and J. Lu, Tunable Bandgap in Silicene and Germanene, Nano Lett. **12**, 113 (2012).

[42] P. Vishnoi, K. Pramoda, and C. N. R. Rao, 2D elemental nanomaterials beyond graphene, ChemNanoMat **5**, 1062 (2019).

[43] D. Geng and H. Y. Yang, Recent advances in growth of novel 2D materials: Beyond graphene and transition metal dichalcogenides, Adv. Mater. **30**, 1800865 (2018).

[44] F. Wang, Z. Wang, L. Yin, R. Cheng, J. Wang, Y. Wen, T. A. Shifa, F. Wang, Y. Zhang, X. Zhan, and J. He, 2D library beyond graphene and transition metal dichalcogenides: A focus on photodetection, Chem. Soc. Rev. **47**, 6296 (2018).

[45] B. Liu and K. Zhou, Recent progress on graphene-analogous 2D nanomaterials: Properties, modeling and applications, Prog. Mater. Sci. **100**, 99 (2019).

[46] K. S. Novoselov, A. K. Geim, S. V. Morozov, D. Jiang, M. I. Katsnelson, I. V. Grigorieva, S. V. Dubonos, and A. A. Firsov, Two-dimensional gas of massless Dirac fermions in graphene, Nature (London) **438**, 197 (2005).

[47] A. H. Castro Neto, F. Guinea, N. M. R. Peres, K. S. Novoselov, and A. K. Geim, The electronic properties of graphene, Rev. Mod. Phys. **81**, 109 (2009).

[48] T. Stauber, N. M. R. Peres, and A. K. Geim, Optical conductivity of graphene in the visible region of the spectrum, Phys. Rev. B **78**, 085432 (2008).

[49] G. B. Ventura, D. J. Passos, J. M. B. Lopes dos Santos, J. M. Viana Parente Lopes, and N. M. R. Peres, Gauge covariances and nonlinear optical responses, Phys. Rev. B **96**, 035431 (2017).

[50] D. J. Passos, G. B. Ventura, J. M. Viana Parente Lopes, J. M. B. Lopes dos Santos, and N. M. R. Peres, Nonlinear optical responses of crystalline systems: Results from a velocity gauge analysis, Phys. Rev. B **97**, 235446 (2018).

[51] R. W. Boyd, *Nonlinear Optics*, 4th ed. (Academic Press, San Diego, CA, 2020).

[52] A. Taghizadeh, K. S. Thygesen, and T. G. Pedersen, Two-dimensional materials with giant optical nonlinearities near the theoretical upper limit, ACS Nano **15**, 7155 (2021).

[53] E. J. Sie, *Coherent Light-Matter Interactions in Monolayer Transition-Metal Dichalcogenides*, 1st ed. (Springer, Basel, Switzerland, 2018).

[54] J. E. Moore and J. Orenstein, Confinement-Induced Berry Phase and Helicity-Dependent Photocurrents, Phys. Rev. Lett. **105**, 026805 (2010).

[55] S. M. Young and A. M. Rappe, First Principles Calculation of the Shift Current Photovoltaic Effect in Ferroelectrics, Phys. Rev. Lett. **109**, 116601 (2012).

[56] I. Sodemann and L. Fu, Quantum Nonlinear Hall Effect Induced by Berry Curvature Dipole in Time-Reversal Invariant Materials, Phys. Rev. Lett. **115**, 216806 (2015).

[57] M. O. Sauer, A. Taghizadeh, U. Petralanda, M. Ovesen, K. S. Thygesen, T. Olsen, H. Cornean, and T. G. Pedersen, Shift current photovoltaic efficiency of 2d materials, npj Comput. Mater. **9**, 35 (2023).

[58] G. B. Ventura, Nonlinear optical response of two-dimensional crystals, Ph.D. Thesis, Department of Physics and Astronomy, University of Porto, 2021.

[59] A. Taghizadeh and T. G. Pedersen, Nonlinear optical selection rules of excitons in monolayer transition metal dichalcogenides, Phys. Rev. B **99**, 235433 (2019).

[60] D. Xiao, G.-B. Liu, W. Feng, X. Xu, and W. Yao, Coupled Spin and Valley Physics in Monolayers of MoS_2 and Other Group-Vi Dichalcogenides, Phys. Rev. Lett. **108**, 196802 (2012).

[61] J. C. Slater and G. F. Koster, Simplified lcao method for the periodic potential problem, Phys. Rev. **94**, 1498 (1954).

[62] S.-R. Song, J.-H. Yang, S.-X. Du, H.-J. Gao, and B. I. Yakobson, Dirac states from px y orbitals in the buckled honeycomb structures: A tight-binding model and first-principles combined study, Chin. Phys. B **27**, 087101 (2018).

[63] J. C. G. Henriques, I. Epstein, and N. M. R. Peres, Absorption and optical selection rules of tunable excitons in biased bilayer graphene, Phys. Rev. B **105**, 045411 (2022).

[64] S. Di Sabatino, J. A. Berger, and P. Romaniello, Optical spectra of 2D monolayers from time-dependent density functional theory, Faraday Discuss. **224**, 467 (2020).

[65] X. Zhang, W.-Y. Shan, and D. Xiao, Optical Selection Rule of Excitons in Gapped Chiral Fermion Systems, Phys. Rev. Lett. **120**, 077401 (2018).

[66] T. Cao, M. Wu, and S. G. Louie, Unifying Optical Selection Rules for Excitons in Two Dimensions: Band Topology and Winding Numbers, Phys. Rev. Lett. **120**, 087402 (2018).

[67] J. C. G. Henriques, B. Amorim, R. M. Ribeiro, and N. M. R. Peres, Excitonic response of AA′ and AB stacked hBN bilayers, Phys. Rev. B **105**, 115421 (2022).

[68] C. Aversa and J. E. Sipe, Nonlinear optical susceptibilities of semiconductors: Results with a length-gauge analysis, Phys. Rev. B **52**, 14636 (1995).

[69] V. N. Genkin and P. M. Mednis, Contribution to the theory of nonlinear effects in crystals with account taken of partially filled bands, Sov. JETP **27**, 609 (1968).

[70] B. Kirtman, F. L. Gu, and D. M. Bishop, Extension of the Genkin and Mednis treatment for dynamic polarizabilities and hyperpolarizabilities of infinite periodic systems. I. Coupled perturbed Hartree–Fock theory, J. Chem. Phys. **113**, 1294 (2000).

[71] V. A. Margulis, E. E. Muryumin, and E. A. Gaiduk, Optical second-harmonic generation from two-dimensional hexagonal crystals with broken space inversion symmetry, J. Phys.: Condens. Matter **25**, 195302 (2013).

[72] T. G. Pedersen, Intraband effects in excitonic second-harmonic generation, Phys. Rev. B **92**, 235432 (2015).

[73] S. K. Radha, W. R. L. Lambrecht, B. Cunningham, M. Grüning, D. Pashov, and M. van Schilfgaarde, Optical response and band structure of $LiCoO_2$ including electron-hole interaction effects, Phys. Rev. B **104**, 115120 (2021).

[74] K. S. Thygesen, Calculating excitons, plasmons, and quasiparticles in 2D materials and van der Waals heterostructures, 2D Mater. **4**, 022004 (2017).

[75] D. Y. Qiu, T. Cao, and S. G. Louie, Nonanalyticity, Valley Quantum Phases, and Lightlike Exciton Dispersion in Monolayer Transition Metal Dichalcogenides: Theory and First-Principles Calculations, Phys. Rev. Lett. **115**, 176801 (2015).

[76] M. O. Sauer, C. E. M. Nielsen, L. Merring-Mikkelsen, and T. G. Pedersen, Optical emission from light-like and particle-like excitons in monolayer transition metal dichalcogenides, Phys. Rev. B **103**, 205404 (2021).

[77] S. N. Rytova, The screened potential of a point charge in a thin film, Mosc. Un. Phys. Bul. **3**, 18 (1967).

[78] L. V. Keldysh, Coulomb interaction in thin semiconductor and semimetal films, Sov. JETP **29**, 658 (1979).

[79] P. Li and I. Appelbaum, Excitons without effective mass: Biased bilayer graphene, Phys. Rev. B **99**, 035429 (2019).

[80] T. Tian, D. Scullion, D. Hughes, L. H. Li, C.-J. Shih, J. Coleman, M. Chhowalla, and E. J. G. Santos, Electronic Polarizability as the Fundamental Variable in the Dielectric Properties of Two-Dimensional Materials, Nano Lett. **20**, 841 (2020).

[81] F. Wu, F. Qu, and A. H. MacDonald, Exciton band structure of monolayer MoS_2, Phys. Rev. B **91**, 075310 (2015).

[82] C. Y.-P. Chao and S. L. Chuang, Analytical and numerical solutions for a two-dimensional exciton in momentum space, Phys. Rev. B **43**, 6530 (1991).

[83] D. G. W. Parfitt and M. E. Portnoi, The two-dimensional hydrogen atom revisited, J. Math. Phys. **43**, 4681 (2002).

[84] M. F. C. Martins Quintela and N. M. R. Peres, Tunable excitons in rhombohedral trilayer graphene, Phys. Rev. B **105**, 205417 (2022).

[85] A. Taghizadeh and T. G. Pedersen, Gauge invariance of excitonic linear and nonlinear optical response, Phys. Rev. B **97**, 205432 (2018).

[86] G. F. Mkrtchian, A. Knorr, and M. Selig, Theory of second-order excitonic nonlinearities in transition metal dichalcogenides, Phys. Rev. B **100**, 125401 (2019).

[87] X.-J. Ge, K.-L. Yao, and J.-T. Lü, Comparative study of phonon spectrum and thermal expansion of graphene, silicene, germanene, and blue phosphorene, Phys. Rev. B **94**, 165433 (2016).

[88] Y. Xu, B. Peng, H. Zhang, H. Shao, R. Zhang, and H. Zhu, First-principle calculations of optical properties of monolayer arsenene and antimonene allotropes, Ann. Phys. (NY) **529**, 1600152 (2017).

[89] Y. Chen, Q. Sun, and P. Jena, SiTe monolayers: Si-based analogues of phosphorene, J. Mater. Chem. C **4**, 6353 (2016).

[90] J. C. G. Henriques, G. B. Ventura, C. D. M. Fernandes, and N. M. R. Peres, Optical absorption of single-layer hexagonal boron nitride in the ultraviolet, J. Phys.: Condens. Matter **32**, 025304 (2020).

[91] M. F. C. M. Quintela, J. C. G. Henriques, L. G. M. Tenório, and N. M. R. Peres, Theoretical Methods for Excitonic Physics in 2D Materials, Phys. Status Solidi B **259**, 2200097 (2022).

[92] D. A. Kleinman, Theory of second harmonic generation of light, Phys. Rev. **128**, 1761 (1962).